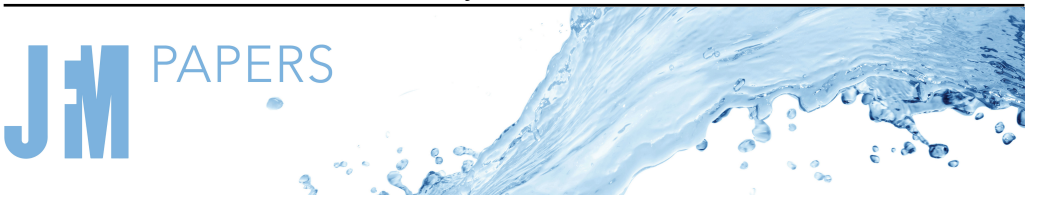
J. Fluid Mech. (2026), *vol.* 1036, A37, doi:10.1017/jfm.2026.11650



Interaction between an in-flow particle and phase change

Jacob Marcus Jepson[1] and **Frank T. Smith**[1]

[1]Department of Mathematics, University College London, London, UK

Corresponding author: Jacob Marcus Jepson, jacob.jepson@ucl.ac.uk

(Received 11 November 2025; revised 30 April 2026; accepted 6 May 2026)

The motion of a rigid particle which is in flight close to a solidifying or melting wall-embedded substrate is modelled for unsteady planar flow. The particle as well as the particle–substrate gap width are modelled as thin, which allows the equations governing fluid flow to be reduced to thin-layer form. The small Prandtl number limit is also exploited, which allows the fluid temperature to be obtained in closed form. Numerical simulations of the interactive system reveal four types of terminal solution behaviour, namely a collision (strictly near collision) between the substrate boundary and front, middle or back of the particle, or a fly-away phenomenon as the particle departs comparatively far from the substrate. For the case of a mid-body collision, a local analysis reveals an intricate asymptotic structure for the model solutions. The case of a rigid substrate and melting or solidifying particle is also examined.

Key words: particle/fluid flows

1. Introduction

Particle–wall interactions in fluid flow occur in many practical settings and are of particular interest at moderate to high Reynolds numbers. Examples include debris removal (Godone & Stanchi 2011), ski and aircraft take-off (Virmavirta, Kivekas & Komi 2001), leaf blowing and saltation (Owen 1964; Shao, Raupach & Findlater 1993; Foucaut & Stanislas 1997), food sorting, sand motion and aircraft icing (Gent, Dart & Cansdale 2000; Purvis & Smith 2016; Norde 2017). Theoretical and experimental studies for moving particles of fixed shape in fluid flow at medium to high Reynolds numbers

© The Author(s), 2026. Published by Cambridge University Press. This is an Open Access article, distributed under the terms of the Creative Commons Attribution licence (https://creativecommons.org/licenses/by/4.0/), which permits unrestricted re-use, distribution and reproduction, provided the original article is properly cited.

https://doi.org/10.1017/jfm.2026.11650 Published online by Cambridge University Press

include those by Coulson and Richardson (2019) and Will *et al.* (2021). Further theoretical analyses of fixed-shape particles in such flows include Smith (2017) and Palmer & Smith (2020), while flexible particles have been considered by Pei, Zhang & Zhou (2018) and Dotto, Soldate & Marchioli (2019). Of more relevance are applications where phase change accompanies the fluid motion, as in aircraft, marine and engine icing. In these systems, a particle or wall patch may act as a local site of melting or solidification, driven by heat transfer between the solid and fluid phases (Gent *et al.* 2000; Norde 2017). Application to another area, namely the flow of liquid metals containing particles or impurities, is of special interest here.

The main body of this paper seeks to investigate the coupled motion of an inviscid fluid and a freely moving rigid particle which is in flight close to a substrate which can melt or solidify. The substrate is embedded within a solid wall, and can either accrete material that creates a hump or melt away and create a cavity. The particle is nearly aligned with the surrounding wall which is taken to be locally flat. The substrate and surrounding fluid are composed of the same material and are taken to have nearly equal densities. The particle, being hotter or colder than the ambient fluid, serves as a finite heat source or sink, inducing melting or solidification of the nearby substrate. The fluid flow couples with the particle motion via the pressure forces acting on the particle surface. In addition, however, the consequent alteration in the shape of the fluid-filled gap between the wall and the particle surface enhances or decreases the thermal transfer effect, showing that the phase change is dependent on the fluid flow, as well as *vice versa*. This work seeks to investigate how the particle geometry and the substrate–particle temperature difference influence the particle trajectory and the evolution of the substrate boundary position.

The model described above for a rigid particle and phase-changing substrate can be readily adapted to the case of a rigid substrate and a phase-changing particle. This scenario is discussed in Appendix A, and shows that heating or cooling of the fixed substrate induces particle melting or fluid solidification, respectively. The particle thus changes shape, thereby altering the fluid dynamics and the heat transfer as well as the particle motion. This particular application is of industrial interest due to the possible potential improvements in efficiency achieved by suitably adjusting or intermittently turning off the substrate heating, enough to prevent particles impacting on the wall.

In this work, we consider a regime in which the Reynolds number based on the particle length is large and the Prandtl number is small. The characteristic time scales associated with substrate phase change and fluid motion are assumed to be comparable, so that unsteady effects due to particle melting/solidification and the hydrodynamics are fully coupled. The densities of the fluid and solid phases are taken to be comparable (as is physically relevant when both phases consist of the same material) and, for simplicity, are hence assumed equal throughout the analysis. The above assumptions are most consistent with metallic systems (Zwirner & Shishkina 2018; Kalantar-Zadeh, Rahim & Tang 2021; Kim *et al.* 2024; Krishnamurthi *et al.* 2024), as will be shown later in § 2, where representative parameter values are presented. In particular, they correspond to situations in which a liquid metal flows over a substrate and a boundary layer forms, see Bian & Rangel (1996) and Lofgren (2001) for example, and background studies by Katgerman (1988), Kurz & Fisher (1992), Carpenter & Steen (1997), Steen & Karcher (1997), Löfgren & Åkerstedt (1998) and Nyström *et al.* (2003). In this setting, the particle is interpreted as a solid impurity within the liquid metal, and for tractability the particle thickness is comparable to the width of the fluid gap between the particle and wall (Wilson & Smith 2011; Jolley & Smith 2024). The fluid is assumed inviscid and incompressible and the flow to be laminar and unsteady in two dimensions.

https://doi.org/10.1017/jfm.2026.11650 Published online by Cambridge University Press

Concerning comparisons with existing recent theoretical studies, the current modelling is similar to that in Jolley & Smith (2024) in the sense that the density ratio is $\mathcal{O}(1)$, but incorporation of phase-change effects is a major novel feature here. Other analytical works on fluid/particle interactions for large Reynolds numbers (Wilson & Smith 2011; Palmer & Smith 2020; Liu, Yazar & Smith 2023) are usually valid only for large density ratios and in many cases take the flow to be quasi-steady, unlike in the present work.

The remainder of the paper is constructed as follows. In § 2, the governing equations are presented and the reduced model is formulated. In § 3, we then present and discuss numerical solutions of the model which illustrate four types of terminal behaviour: a collision (strictly near collision) between the substrate boundary and front, middle or back of the particle, or a fly-away phenomenon as the particle departs comparatively far from the substrate. The asymptotic structure of solutions in the case of a mid-body collision is presented in § 4. Conclusions and discussions follow in § 5.

2. Governing equations

Our main concern is with the scenario of a thin rigid in-flow particle positioned above a wall-embedded substrate whose boundary can evolve due to phase change. A schematic of the model geometry is provided in figure 1. The interaction considered involves melting or accretion of the substrate due to the comparatively hot or cold particle. The resulting change in the fluid gap between the particle and substrate alters the hydrodynamic forces on the particle, which in turn feeds back on the fluid temperature and the substrate melting rate. This three-way interaction between fluid flow, particle motion and phase change is nonlinear in general. The underlying equations are the continuity and Navier–Stokes equations for the fluid motion, those of rigid-particle motion for the particle and a thermal equation for the fluid temperature. These are coupled with a Stefan condition which determines the position of the substrate. The particle is modelled as thin, lying close to (and almost aligned with) a straight fixed wall and moving in the presence of an incident uniform stream of fluid with streamwise velocity U^*. The asterisk denotes a dimensional quantity.

The fluid in question is composed of the same material as the substrate. Consequently, the fluid and solid densities are comparable, and in the present work we take them to be identical, denoted by ρ^*. The characteristic gap width W^* between the substrate and the particle underbody is small compared with the particle length L^* in the streamwise direction (Smith & Ellis 2010; Wilson & Smith 2011; Jolley & Smith 2024). We work with dimensionless distances, velocities, times and pressures which are scaled with L^*, U^*, L^*/U^* and ρU^{*2}, respectively, together with the ratio $W^*/L^* := \varepsilon \ll 1$ being small. The time scales of the fluid flow and the phase change are assumed comparable. The fluid is taken to be not only incompressible but also inviscid in effect, which is justified provided ε is large compared with the typical boundary layer thickness, which is of order $Re^{-1/2}$ where the Reynolds number Re is based on the particle length. The overall interaction is modelled as two-dimensional in the $L^*(x,\ \varepsilon y)$ plane, where x and y describe the dimensionless longitudinal and lateral position. The corresponding unknown fluid velocity and pressure are $U^*(u,\ \varepsilon v)$ and $\rho^* U^{*2} p$, where $u,\ v$ denote the longitudinal and lateral dimensionless velocity components and p the dimensionless pressure. The particle occupies the interval $0 < x < 1$ and its angles of inclination during its motion are assumed to be of order ε, the same as those of the fluid-filled gap. As in Jolley & Smith (2024), the particle overbody shape can also be specified, however, provided it remains thin it does not contribute to the leading-order interaction as the corresponding induced pressure variation is small compared with that of the underbody.

https://doi.org/10.1017/jfm.2026.11650 Published online by Cambridge University Press

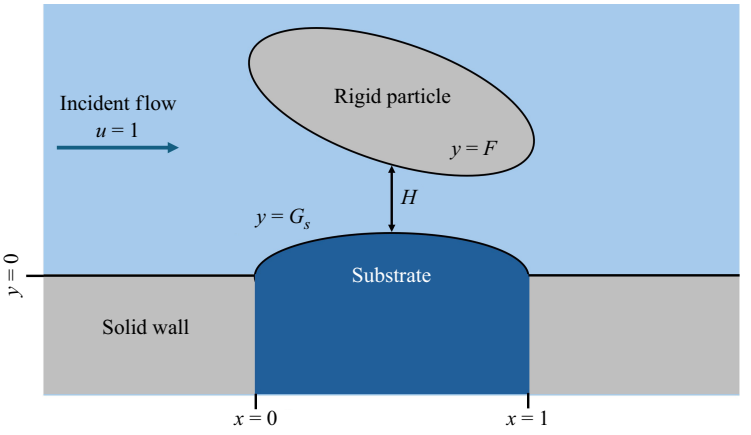


Figure 1. A schematic illustrating the dimensionless model geometry, where $H(x,\ t)$ denotes the gap width and $y = F(x,\ t)$, $G_s(x,\ t)$ describe the position of rigid-particle underbody and substrate boundary.

As discussed in § 1, the assumptions outlined in the introduction and the preceding paragraph are consistent with liquid-metal flows, and parameter value estimates are now discussed to justify this. Typical material properties for molten metals are a dynamic viscosity of order $\mu^* \approx 10^{-3}$ Pa s and a density of $\rho^* \approx 5 \times 10^3$ kg m^{-3} (Dinsdale & Quested 2004). We take the characteristic velocity scale to be $U^* \approx 10^{-1}$ m s^{-1}, consistent with reported molten steel flow velocities in industrial casting processes (Zhang, Yang & Jiang 2019); see also Lofgren (2001). Taking the characteristic particle length (interpreted here as an impurity within the flowing metal) to be $L^* \approx 10^{-2}$ m, the corresponding Reynolds number $Re = \rho^* U^* L^*/\mu$ is $Re \approx 5 \times 10^3$, which justifies the large Re assumption taken in this work. As noted above, viscous effects are negligible provided $Re^{-1/2} \ll \varepsilon$. For the representative values of L^* and Re above, this condition suggests that the present analysis can apply when $W^* \approx 1.4 \times 10^{-3}$ m, corresponding to $\varepsilon \approx 1.4 \times 10^{-1}$. For liquid-metal flows, the Prandtl number is typically small. Using values for the kinematic viscosity which is calculated from μ and ρ^* above alongside a thermal diffusivity of $\alpha^* \approx 2 \times 10^{-5}$ m^2 s^{-1} (Stankus, Savchenko & Agazhanov 2012) gives the Prandtl number $\sigma = \mu^*/(\rho^*\alpha^*)$ as $\sigma \approx 10^{-2}$, thus suggesting the small σ limit exploited subsequently. Using the above values, the characteristic flow time scale, L^*/U^*, is approximately 0.1 s. On the other hand, the phase-change time scale, $W^{*2}/(\alpha^* St)$, where $St = c_p \Delta T/L_f$ is the Stefan number (with c_p, ΔT and L_f denoting the specific heat, temperature variation and latent heat, respectively), is also 0.1 s provided that $St \approx 1$. This justifies the assumption that the solidification and flow time scales are comparable.

The equations governing the fluid flow, given the above assumptions on particle and fluid slenderness, and the absence of any incident vorticity (since the incident flow has $u = 1$ and $v = 0$), reduce to the thin-layer form

$$\frac{\partial H}{\partial t} + \frac{\partial}{\partial x}(uH) = 0, \tag{2.1a}$$

$$\frac{\partial u}{\partial t} + u\frac{\partial u}{\partial x} = -\frac{\partial p}{\partial x}, \tag{2.1b}$$

where H is the scaled unknown gap width between the substrate boundary and particle underbody. The corresponding scaled gap pressure p is of order unity and satisfies the Bernoulli constraint at the particle leading edge where $x = 0$ and the Kutta condition at

https://doi.org/10.1017/jfm.2026.11650 Published online by Cambridge University Press

the trailing edge where $x = 1$, so that

$$p = \frac{1}{2}\left(1 - u^2\right) \quad \text{at} \quad x = 0, \tag{2.2a}$$

$$p = 0 \quad \text{at} \quad x = 1. \tag{2.2b}$$

We note there are thin viscous layers present on the particle surfaces which are assumed separation free. Concerning the Kutta condition from (2.2*b*), we note in addition that, and in contrast with the $\mathcal{O}(1)$ pressures in the gap, the pressure contributions above the particle are negligible to leading order ε, in view of the fluid flow slenderness and the $\mathcal{O}(\varepsilon)$ particle slopes. We now consider the remaining two components of the interaction, namely the particle motion and substrate phase change.

Denoting the position of the unknown substrate boundary and particle underbody as $y = G_s(x,\ t)$ and $y = F(x,\ t)$, respectively, the fluid-filled gap width is then given by $H = F - G_s$. As discussed above, the particle overbody motion does not contribute to the leading-order interaction and is hence neglected here. The case of $G_s < 0$ corresponds to scenario where the substrate boundary has melted beneath the wall at $y = 0$, whereas $G_s > 0$ represents ice accretion in the form of a hump. We suppose that $F = F_p(x) + h(t) + (x - \beta)\theta(t)$ such that F_p is the given shape of the particle underbody, whereas $h(t)$ and $\theta(t)$ describe the unknown lateral and rotational particle position, respectively. Here, $x = \beta$ denotes the prescribed position of the particle centre of mass. To clarify, the function $h(t)$ represents the scaled time dependence of the y-coordinate of the centre of mass, which is fixed within the particle. Its horizontal motion is negligible to leading order in ε. In view of the above relations, we have that

$$H = G(x,\ t) + h_c(t) + x\theta(t), \tag{2.3}$$

where $G = F_p(x) - G_s(x,\ t)$ and $h_c = h - \beta\theta$. It is assumed that the particle underbody shape and the evolving substrate boundary shape are relatively smooth and their slopes are not too extreme. Otherwise flow separation may occur in the thin viscous boundary layers on the underbody and on the substrate, either locally to, say, a discontinuity in slope or globally: the latter global separation would require re-modelling of the flow.

The equations governing the motion of the rigid particle, and hence evolution of $h(t)$ and $\theta(t)$ require a balance between mass-acceleration effects and fluid-pressure forces. In the present situation of a near-wall slender particle of density comparable to that of the surrounding fluid, a scaling argument indicates that forces induced by the fluid pressure dominate the mass-acceleration terms. Hence, particle motion is governed by (Jolley & Smith 2024)

$$\int_0^1 p\,\mathrm{d}x = \int_0^1 xp\,\mathrm{d}x = 0, \tag{2.4}$$

corresponding to a configuration where the so-called added mass is dominant over the actual particle mass. We note that the argument of the second integral here is strictly $(x - \beta)$, although the first integral is used to reduce it to its current form.

The particle and substrate are assumed to have uniform density, with the substrate boundary temperature taken as the melt temperature, which is normalised to zero. The dimensional fluid temperature is written as $T^* = T_m^* + (T_w^* - T_m^*)T$, where T_m^* and T_w^* denote the characteristic dimensional melting and particle temperature, respectively. The dimensionless fluid temperature $T(x,\ y,\ t)$ is governed by the thermal transport equation

https://doi.org/10.1017/jfm.2026.11650 Published online by Cambridge University Press

$$\frac{\partial T}{\partial t}+u\frac{\partial T}{\partial x}+v\frac{\partial T}{\partial y}=\frac{1}{\varepsilon^2 Re\,\sigma}\frac{\partial^2 T}{\partial y^2}, \tag{2.5}$$

where σ is the Prandtl number. Dissipation effects are neglected here as in Moore, Mughal & Papageorgiou (2017), Jepson, Batley & Smith (2025) and Batley & Smith (2025), on account of the representative thermal range associated with θ dominating over the speed range proportional to u^2. We assume that the particle underbody temperature is prescribed as $T_p(x,\ t)$, where $T_p>0$ or $T_p<0$ is expected to relate to melting or solidification of the wall-mounted substrate. Recalling that the substrate boundary temperature is zero, the boundary conditions on T are thus

$$T=0 \qquad \text{at} \quad y=G_s, \tag{2.6a}$$

$$T=T_p \qquad \text{at} \quad y=F. \tag{2.6b}$$

The temperature beneath the substrate is assumed to be zero in this paper, which points to the heat flux within the substrate being negligible. The position of the melting or solidifying substrate, to leading order in ε, is then governed by the Stefan condition

$$\frac{\partial G_s}{\partial t}=-b\frac{\partial T}{\partial y} \qquad \text{at} \quad y=G_s, \tag{2.7}$$

where the constant $b>0$ is directly proportional to the Stefan number.

In view of the parameter values discussed above, we now take the small Prandtl number limit $\sigma \ll \varepsilon^{-2}Re^{-1}$, so that the left-hand side of (2.5) is negligible, leaving the right-hand side equating zero. The thermal response is thus distinct from the flow response in the sense that the convection effects alone are not significant in the gap (unlike the inertial contributions in the fluid flow). Using the boundary conditions from (2.6), we hence obtain to leading order

$$T=\frac{T_p}{H}(y-G_s), \tag{2.8}$$

so that the Stefan condition from (2.7) provides

$$\frac{\partial G_s}{\partial t}=-b\frac{T_p}{H}, \tag{2.9}$$

which relates the evolution of the substrate shape directly to the local wall temperature and the local gap width.

The coupling of the fluid flow, particle motion and fluid temperature is captured by the system (2.1)–(2.4) and (2.9). These equations are subject to initial conditions on the substrate G_s and the mass flux entering the gap at $x=0$, as well as on h, θ and their first derivatives. The necessity and application of these conditions is seen more clearly in the following section. In general the system described above is nonlinear and must be solved numerically, as described in the next section. It is found subsequently that the computational results point to further analysis and insight.

3. Numerical results

In this section, the numerical solutions of the interactive system from (2.1)–(2.4) and (2.9) are discussed, paying particular attention to exemplar parameter values whereby solutions indicate a trailing-edge, leading-edge and mid-body impact between the particle and substrate, and a particle fly-away response. Before this, we discuss the numerical methods used to solve the interactive system.

https://doi.org/10.1017/jfm.2026.11650 Published online by Cambridge University Press

3.1. *Numerical methods*

By integrating (2.1*a*) in x we obtain

$$u = -\frac{1}{H}\left[\int_0^x \frac{\partial H}{\partial t}\,\mathrm{d}\xi + A(t)\right], \tag{3.1}$$

such that $-A(t)$ denotes the scaled mass flux entering the gap for any t at $x = 0$. Now, integrating (2.1*b*) over x and imposing (2.2) provides

$$\int_0^1 \frac{\partial u}{\partial t}\,\mathrm{d}x = L(t), \tag{3.2a}$$

where $L(t) = 1/2(1 - u^2(1,\ t))$. Similarly, by multiplying (2.1*b*) by x and then x^2, integrating over x and then using the lift and moment equations from (2.4), we obtain

$$\int_0^1 x\frac{\partial u}{\partial t}\,\mathrm{d}x = \frac{1}{2}\int_0^1 u^2\,\mathrm{d}x - \frac{1}{2} + L(t), \tag{3.2b}$$

$$\int_0^1 x^2\frac{\partial u}{\partial t}\,\mathrm{d}x = \int_0^1 xu^2\,\mathrm{d}x - \frac{1}{2} + L(t). \tag{3.2c}$$

The pressure is obtained explicitly in terms of u by integrating (2.1*b*) in x and using (2.2*a*), so that

$$p = -\int_0^x \frac{\partial u}{\partial t}\,\mathrm{d}\xi - \frac{u^2}{2} + \frac{1}{2}. \tag{3.3}$$

The contributions of u and its first derivative in t seen in the integral system above from (3.2) are obtained by differentiating (3.1) with respect to t and then substituting H from (2.3). Denoting $' \equiv (\partial/\partial t)$ for clarity, we have

$$u = -\frac{x^2\omega + 2(I + vx + A)}{2H}, \tag{3.4a}$$

$$\frac{\partial u}{\partial t} = \frac{H'\left(x^2\omega + 2(I + vx + A)\right)}{2H^2} - \frac{x^2\omega' + 2(J + v'x + A')}{2H}, \tag{3.4b}$$

where $v = h_c'$ and $\omega = \theta'$, and

$$I(x,\ t) = b\int_0^x \frac{T_p}{H}\,\mathrm{d}\xi, \tag{3.4c}$$

$$J(x,\ t) = b\int_0^x \frac{T_p'H - H'T_p}{H^2}\,\mathrm{d}\xi. \tag{3.4d}$$

We note that $H' = bT_p/H + v + x\omega$, in view of (2.3) and (2.9).

Using the relations from (3.4), the integral equations from (3.2) are arranged into a system of three nonlinear ordinary differential equations in t, explicitly for $v'(t)$, $\omega'(t)$ and $A'(t)$. This couples the equations $h_c'(t) = v$ and $\theta'(t) = \omega$, as well as the Stefan condition from (2.9) for $G_s'(t)$. This forms a system of six equations for the unknowns $(h_c,\ \theta,\ v,\ \omega,\ A,\ G_s)$ and their corresponding initial states at $t = 0$. The spatial integral terms were obtained via the function `cumtrapz` in MATLAB using 10^4 grid points. Numerical convergence was verified by independent grid refinement, which showed the solution to be insensitive to further refinement well below the number of grid points used. The time derivatives were integrated via the function `ode45` in MATLAB, which employs an adaptive Runge–Kutta method.

https://doi.org/10.1017/jfm.2026.11650 Published online by Cambridge University Press

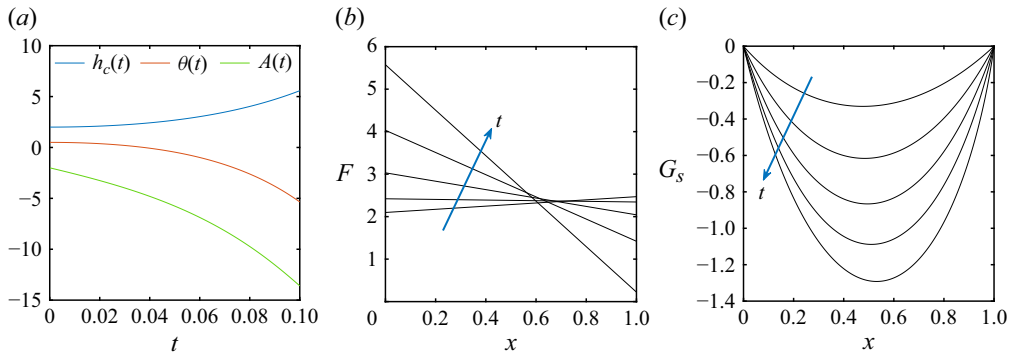


Figure 2. Numerical results of the interactive system from (3.2) and (2.9) for $b = 80$, $\alpha = 2$ and $F_p(x) = 0$. Panel (a) shows the total lateral and rotational position, $h_c(t)$ and $\theta(t)$, and the mass flux $A(t)$. Panels (b) and (c) show the particle underbody and substrate boundary position for five uniformly distributed values of $t \in [0.02,\ 0.1]$. The arrows point in the increasing direction of t. The initial conditions are taken as $G_s(x,\ 0) = 0$ and $(h_c,\ \theta,\ v,\ \omega,\ A) = (2,\ 1/2,\ 0,\ 0,\ -2)$.

3.2. *Results*

As previously mentioned, we now present and discuss numerical solutions of the interactive system, governed by the integral system from (3.2) and the Stefan condition from (2.9). Throughout this section, we take the particle temperature to be $T_p = \alpha x(1 - x)$ for $\alpha \in \mathbb{R}$, and take the initial substrate shape to be flat, so that $G_s(x,\ 0) = 0$, and set $(h_c,\ \theta,\ v,\ \omega,\ A) = (2,\ 1/2,\ 0,\ 0,\ -2)$. We focus on varying the values of α, the phase-change parameter b and the position of the particle underbody $y = F_p(x)$ in order to generate contrasting solution behaviour.

In figure 2, results are presented for a flat particle underbody $(F_p(x) = 0)$ with $b = 80$ and $\alpha = 2$, the latter corresponding to a relatively hot particle. In this case, the position of the particle leading and trailing edges are seen to monotonically increase and decrease in t, respectively (figure 2b). This leads to an eventual positive incidence of the particle body, and then impact of the particle trailing edge with the substrate at $x = 1$. We note that, strictly speaking, the model predicts only near impact, as new physical effects must arise as the gap width approaches zero. The total particle lift and rotational position, $h_c(t)$ and $\theta(t)$, are seen to monotonically increase and decrease respectively in figure 2a which is commensurate with the results observed in figure 2b. Furthermore, the mass flux associated with A at $x = 0$ becomes increasingly negative due to the increasing gap width there. In figure 2(c), G_s becomes increasingly negative with t, corresponding to the progressive melting of the substrate caused by the relatively warm particle temperature. The specific shape of G_s is due to the quadratic nature of the particle temperature, and the minimum of G_s at the last value of t shown is very slightly right of the midpoint $(x = (1/2))$ due to the positive incidence of the particle.

In contrast, the results presented in figure 3 represent a cold particle where $\alpha = -2$ is taken. Here, the wall substrate accretes material, with G_s increasing almost symmetrically for the first four values of t shown (figure 3b). Hence, the particle underbody is forced away from the wall and positive incidence is produced, as further illustrated by the functions $h_c(t)$ and $\theta(t)$ in figure 3(a). This evolution leads to a near mid-body collision at $x \approx 0.58$ between the substrate and particle. A striking feature of this case is the pressure profile, which shows a large peak about the location of near impact and negative troughs on either side (figure 3c). We note that the case of $\alpha = 0$, which represents a particle fixed at the melt temperature, gives $G_s = 0$ for all t due to the lack of thermal influence. Results for

https://doi.org/10.1017/jfm.2026.11650 Published online by Cambridge University Press

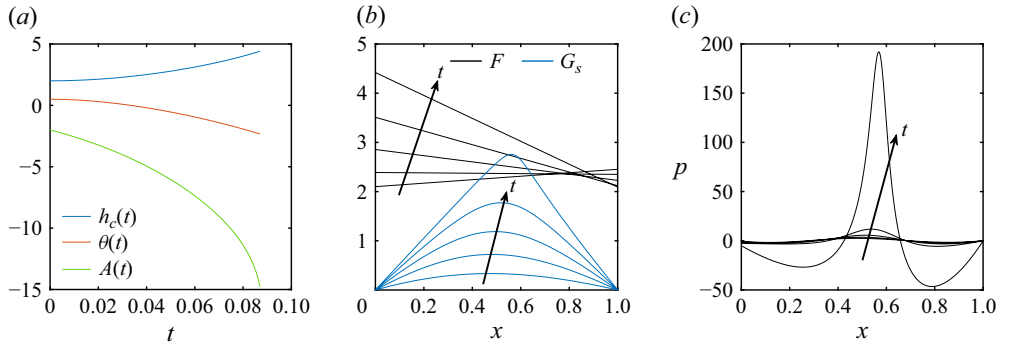


Figure 3. Numerical results of the interactive system from (3.2) and (2.9) for $b = 80,\ \alpha = -2$ and $F_p(x) = 0$. Panel (a) shows the total lateral and rotational position, $h_c(t)$ and $\theta(t)$, and the mass flux $A(t)$. Panel (b) shows the particle underbody and substrate boundary position, whilst (c) shows the pressure from (3.3), for five uniformly distributed values of $t \in [0.17,\ 0.87]$. The arrows point in the increasing direction of t. The initial conditions are taken as $G_s(x,\ 0) = 0$ and $(h_c,\ \theta,\ v,\ \omega,\ A) = (2,\ 1/2,\ 0,\ 0,\ -2)$.

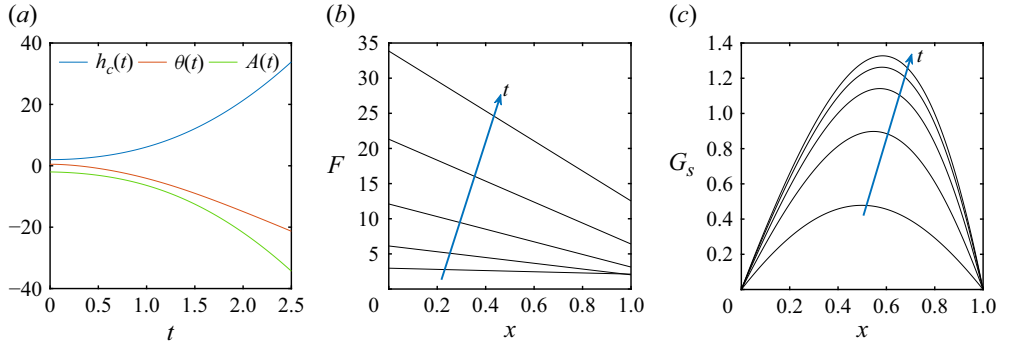


Figure 4. Numerical results of the interactive system from (3.2) and (2.9) for $b = 4,\ \alpha = -2$ and $F_p(x) = 0$. Panel (a) shows the total lateral and rotational position, $h_c(t)$ and $\theta(t)$, and the mass flux $A(t)$. Panels (b) and (c) show the particle underbody and substrate boundary position for five uniformly distributed values of $t \in [0.5,\ 2.5]$. The arrows point in the increasing direction of t. The initial conditions are taken as $G_s(x,\ 0) = 0$ and $(h_c,\ \theta,\ v,\ \omega,\ A) = (2,\ 1/2,\ 0,\ 0,\ -2)$..

this case are therefore not shown here, although the particle retains its negative incidence and an impact again takes place but at the leading edge.

The case in figure 4 now has $b = 4$ and $\alpha = -2$, corresponding to cold particle and a much slower substrate shape evolution than the cases considered above (the same effect is produced alternatively by reducing the magnitude of the temperature difference while keeping b fixed, in view of the condition from (2.7)). The results presented in figure 4(c) shows that the substrate accretes material but grows only relatively slowly due to the reduced value of b; consequently, the particle underbody is ultimately forced away from the wall (due to the oncoming fluid) without an impact occurring. Instead, a fly-away event takes place where, under the positive incidence generated, the particle edges both depart indefinitely from the wall. In view of this, the influence of the particle temperature on the substrate weakens and the growth rate of G_s reduces substantially. The mass flux $A(t)$ also continues to decrease, due to the increasing width between the substrate and particle underbody.

https://doi.org/10.1017/jfm.2026.11650 Published online by Cambridge University Press

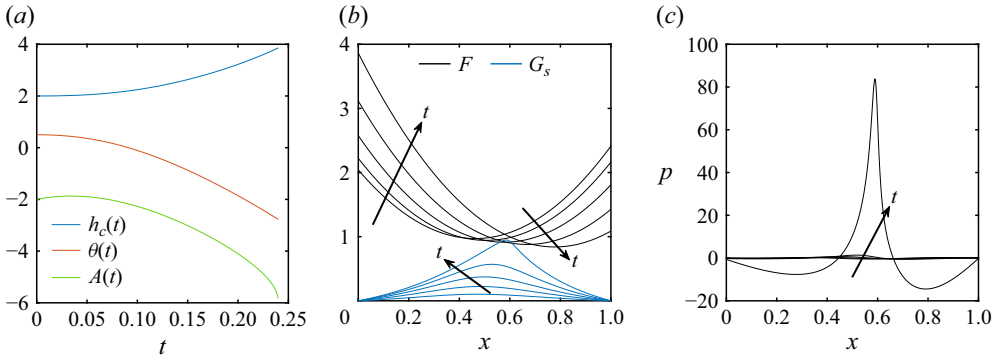


Figure 5. Numerical results of the interactive system from (3.2) and (2.9) for $b = 4$, $\alpha = -2$ and $F_p(x) = -5x(1-x)$. Panel (a) shows the total lateral and rotational position, $h_c(t)$ and $\theta(t)$, and the mass flux $A(t)$. Panel (b) shows the particle underbody and substrate boundary position, whilst (c) shows the pressure from (3.3), for five uniformly distributed values of $t \in [0.048,\ 0.24]$. The arrows point in the increasing direction of t. The initial conditions are taken as $G_s(x,\ 0) = 0$ and $(h_c,\ \theta,\ v,\ \omega,\ A) = (2,\ 1/2,\ 0,\ 0,\ -2)$.

In contrast to the cases presented above, we now consider in figure 5 the particle underbody to have shape $F_p(x) = kx(1-x)$ with $k \in \mathbb{R}$; the other values chosen are equivalent to the above scenario. For $k = -5$, the parabolic underbody produces a significantly different interaction and solution behaviour when compared with the flat underbody case shown in figure 4, in that a mid-body collision occurs instead of a fly-away event. The results for this case are broadly similar, in a qualitative sense, to those in figure 3 near the impact point, with the substrate shape varying rapidly in x and the fluid pressure exhibiting a pronounced local peak (figures 5*b* and 5*c*). By comparison, the value $k = -3$ was found to lead to a fly-away event, as in figure 4.

Figures 2, 3, 4 and 5 show that the interactive thermal conditions have a very sensitive effect on particle travel, fluid motions and substrate evolution. They also illustrate the range of possible terminal states for the particle–fluid–substrate interaction evolution: a near impact at the leading edge, trailing edge or in between, within a finite scaled time; or a fly-away event arising at large t. As such, we now examine the asymptotic behaviour of the interactive system from (3.2) and (2.9) when a particle–substrate collision or fly-away event occurs.

4. Particle–substrate impact or fly-away solutions

The impacts between the particle leading/trailing edge and the substrate (see figure 2), as well as the fly-away response (see figure 4), are all found to be dominated by the fluid–particle interaction, in which thermal effects do not contribute to the leading-order analysis. Of course, however, thermal effects will influence the type of terminal behaviour eventually observed. The local analysis employed to analyse solutions corresponding to leading-/trailing-edge impacts are essentially the same as those analysed in Smith & Ellis (2010), Wilson & Smith (2011) and Jolley & Smith (2024). For fly-away solutions, the gap width H and lateral position h grow linearly in t, whereas θ tends to an $\mathcal{O}(1)$ negative value (giving the negative particle incidence). The flow velocity and pressure behave like $1 + \mathcal{O}(t^{-1})$ and $\mathcal{O}(t^{-1})$, respectively, whereas the frozen substrate boundary grows slowly like $\log(t)$.

In contrast to the terminal behaviours discussed above, thermal effects are non-negligible in the local analysis for a mid-body impact between the particle and substrate

https://doi.org/10.1017/jfm.2026.11650 Published online by Cambridge University Press

(see figures 3 and 5). For this scenario, the numerical results for the pressure in § 3 suggest there are three regions to consider. Specifically, one inner region (I) closely surrounding the impact point, and two other outer regions (II, III) which are an $\mathcal{O}(1)$ distance downstream and upstream of the impact point, respectively. In the following analysis, we exploit the small quantities $|x - x_c| \ll 1$ and $\tau = t_c - t \ll 1$, such that $(x_c,\ t_c)$ denotes the spatial-temporal location of the particle–substrate impact, i.e. where $H(x_c,\ t_c) = 0$. In terms of order of magnitudes in region I, we argue that $\partial G_s/\partial t = \mathcal{O}(\tau^{-1/2})$ (analogous to classical Stefan problems), which therefore suggests H and $x - x_c$ being of $\mathcal{O}(\tau^{1/2})$, in view of the relation from (2.3) and Stefan condition from (2.9). In consequence, the kinematic condition from (2.1*a*) yields $u = \mathcal{O}(\tau^{-1/2})$, so that $p = \mathcal{O}(\tau^{-1})$ by virtue of the momentum balance from (2.1b).

In view of the order of magnitude arguments above, we introduce the following scaling and expansions for region I:

$$\xi = \frac{x - x_c}{\tau^{1/2}}, \qquad H \sim \tau^{\frac{1}{2}} H_1(\xi), \qquad G_s \sim G_0 + \tau^{\frac{1}{2}} G_1(\xi), \tag{4.1a}$$

$$h_c \sim h_0 + \tau \log(\tau^{-1}) h_1, \qquad \theta \sim \theta_0 + \tau \log(\tau^{-1}) \theta_1, \tag{4.1b}$$

where $G_0 = G_s(x_c,\ t_c)$, $h_0 = h_c(t_c)$, $\theta_0 = \theta(t_c)$ and h_1, θ_1 are constant. The correction terms of h_c and θ must be of order $\tau \log(\tau^{-1})$ so that they contribute to the solution behaviour in the outer regions I and II, in view of the outer expansion for H given later in (4.9). The leading-order balance arising from (2.3) necessitates that $F_p(x_c) - G_0 + h_0 + x_c\theta_0 = 0$, whilst the order-$\tau^{1/2}$ balance gives

$$H_1 = -G_1 + \mu\xi, \tag{4.2}$$

where $\mu = F_p'(x_c) + \theta_0$. The Stefan condition from (2.9) provides the ordinary differential equation

$$\xi \frac{\mathrm{d}G_1}{\mathrm{d}\xi} - G_1 = \frac{\ell}{\mu\xi - G_1}, \tag{4.3a}$$

where $\ell = -2bT_p(x_c) > 0$, the solution of which is

$$G_1 = \mu\xi - \sqrt{\ell + c\xi^2}, \tag{4.3b}$$

where $c > 0$ is an unknown constant. The large-$|\xi|$ behaviour $G_1 \sim (\mu - \sqrt{c})|\xi|$ is consistent with the expectation that the correction term for G from (4.1*a*) should be $\mathcal{O}(1)$ when $x = x_c \pm \mathcal{O}(1)$ and $\tau \ll 1$.

We expand the velocity and pressure as

$$u \sim \tau^{-\frac{1}{2}} u_1(\xi), \qquad p \sim \Phi(\tau) + \tau^{-1} p_1(\xi), \tag{4.4}$$

where $\Phi(\tau) \gg \tau^{-1}$ is required to facilitate matching with the solutions when $x = x_c \pm \mathcal{O}(1)$ and is obtained shortly. The remaining scalings from (4.4) are required to obtain a full balance in (2.1). As a result of (4.4), and in view of (4.2) and (4.3*b*), we have

$$u_1 = \frac{c_2 + \ell \log\left(\sqrt{c}\xi + \sqrt{\ell + c\xi^2}\right)}{2\sqrt{c(\ell + c\xi^2)}}, \tag{4.5a}$$

$$p_1 = c_3 - \frac{\xi u_1 + u_1^2}{2}, \tag{4.5b}$$

https://doi.org/10.1017/jfm.2026.11650 Published online by Cambridge University Press

where c_2 and c_3 are unknown constants. The limits of (4.5) as $\xi \to \pm\infty$ which are relevant for matching are

$$u_1 \sim \frac{\ell \log(\pm\xi)}{2c\xi} + \frac{D_\pm}{\xi} \qquad \text{as} \qquad \xi \to \pm\infty, \tag{4.6a}$$

$$p_1 \sim \frac{\ell \log(\pm\xi^{-1})}{4c} + c_3 - \frac{D_\pm}{2} \qquad \text{as} \qquad \xi \to \pm\infty, \tag{4.6b}$$

where

$$D_+ = \frac{2c_2 + \ell \log(4c)}{4c}, \qquad D_- = D_+ - \frac{\ell \log(\ell)}{2c}. \tag{4.6c}$$

The function $\Phi(\tau)$ is determined by using (4.6*b*) and observing that p from (4.4) becomes

$$p = \Phi(\tau) + \frac{\ell}{8c}\tau^{-1}\log(\tau) + \mathcal{O}(\tau^{-1}) \tag{4.7}$$

when $x = x_c \pm \mathcal{O}(1)$, whilst u is of order $\log(\tau^{-1})$ there and hence also of this order in the outer regions II and III. As such, we require $p = \mathcal{O}(\tau^{-1})$ in the outer regions in order to balance the first and last terms of (2.1*b*), and so (4.7) implies

$$\Phi(\tau) = -\frac{\ell}{8c}\tau^{-1}\log(\tau). \tag{4.8}$$

The solutions in the outer regions are now discussed.

Far away from the substrate–underbody impact in regions II and III, the substrate shape G_s and the gap width H are necessarily of order unity, whilst the velocity and pressures are of order $\log(\tau^{-1})$ and τ^{-1}, respectively. Focussing on region III now for simplicity, we expand as

$$H \sim \hat{H}_0(x) + \tau\log(\tau^{-1})\hat{H}_1, \qquad G_s \sim \hat{G}_0(x) + \tau\hat{G}_1(x), \qquad u \sim \log(\tau^{-1})\hat{u}_0(x),$$
$$p \sim \tau^{-1}\hat{p}_0(x), \tag{4.9}$$

when $x = x_c + \mathcal{O}(1)$. Here, the functions $\hat{H}_0$ and $\hat{G}_0$ are arbitrary functions determined by the flow history, and are subject to the relation $\hat{H}_0 = F_p - \hat{G}_0 + h_0 + x\theta_0 = 0$. The orders of the correction terms for H and G here are obtained by seeking the fullest balance in (2.1) and (2.9), respectively, in view of the orders of u and p. Given (4.9), we obtain from (2.1) and (2.9)

$$\hat{H}_1 = \frac{\mathrm{d}}{\mathrm{d}x}(\hat{H}_0\hat{u}_0), \qquad \hat{u}_0 = -\frac{\mathrm{d}\hat{p}_0}{\mathrm{d}x}, \qquad \hat{G}_1 = -b\frac{T_w}{\hat{H}_0}. \tag{4.10}$$

In view of (4.3*b*) and (4.6), the leading-order variables introduced in (4.9) are subject to the matching conditions as $x \to x_c^+$

$$\hat{H}_0 \sim \sqrt{c}(x - x_c), \qquad \hat{G}_0 \sim G_0 + (\mu - \sqrt{c})(x - x_c), \tag{4.11a}$$

$$\hat{u}_0 \sim \frac{\ell}{4c(x - x_c)}, \qquad \hat{p}_0 \sim -\frac{k}{4c}\log(x - x_c) + c_3 - \frac{D_+}{2}. \tag{4.11b}$$

The matching conditions as $x \to x_c^-$ for the leading-order solutions in region II are similar to (4.11) but with $|x - x_c|$ and D_- replacing $x - x_c$ and D_+. Also notable is the property of $-A(t)$ being of order $\log(\tau^{-1})$ and positive near the collision time, which indicates non-zero mass flux near the leading edge, in keeping with the results from figure 5.

https://doi.org/10.1017/jfm.2026.11650 Published online by Cambridge University Press

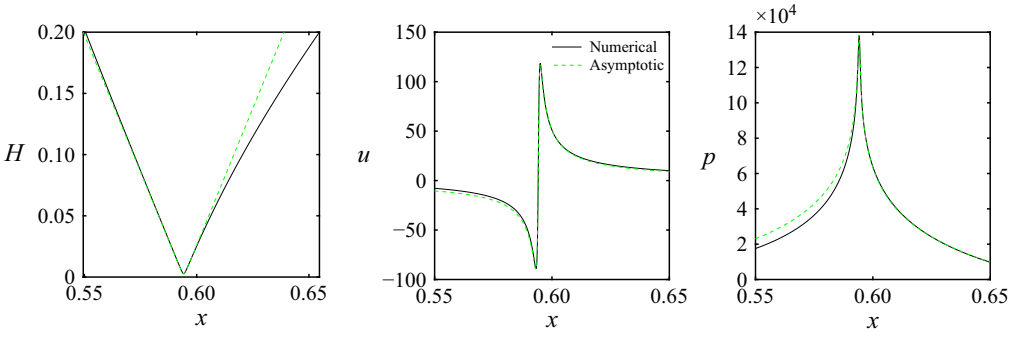


Figure 6. Numerical solutions for $(H,\ u,\ p)$ from the interactive system (3.2) and (2.9) (solid black) compared with the asymptotic solutions from (4.1*a*) and (4.4) (dashed green) at $t = 0.241337$. The parameters selected to obtain the fit between asymptotic and numerical results are $t_c = t + 2 \times 10^{-6},\ x_c = 0.594,\ c = 20,\ c_2 = -2$ and $c_3 = -0.0385$. The initial conditions are taken as $G_s(x,\ 0) = 0$, while $F_p = -5x(1-x),\ \alpha = -2,\ b = 4$ and $(h_c,\ \theta,\ v,\ \omega,\ A) = (2,\ 1/2,\ 0,\ 0,\ -2)$.

Comparisons between the numerical solutions of $H,\ u$ and p against the corresponding asymptotic solutions from (4.1*a*) and (4.4) are provided in figure 6, for the parameter values and constitutive assumptions taken in figure 5. Local to the collision, a favourable agreement between the two solutions is noted. Similar comparisons between the orders of the velocity and pressure in the outer regions are also favourable, although a complete quantitative connection is hampered by the arbitrariness present in the outer-region behaviour.

5. Discussion

In this paper we model the interaction between an in-flow thin rigid particle and the solidification or melting of a solid wall-embedded substrate. The quasi-inviscid fluid in between is of the same material as the substrate in liquid form, while the particle is relatively hot or cold. Numerical computations of the reduced model show quantitatively how the solidifying substrate boundary tends to gradually approach the particle surface if the latter is comparatively cold whereas the substrate melts away in the presence of a hot particle. The evolving change in the lateral gap width between the particle underbody and the substrate affects the fluid flow properties and these in turn influence both the rate of phase change at the substrate boundary and the pressures which control the particle motion.

Four types of terminal solution behaviour have been identified for the nonlinear interaction, the realisation of which depend on the comparative time scales of the fluid flow and the phase change as well as on the original particle shape. Here, the two time scales, of flow and phase change, have been taken to be comparable. Firstly, there can be impact (strictly near impact) upon the substrate, within a finite scaled time, at the particle leading edge, at the trailing edge or at a mid-particle location; alternatively the particle can fly away from the substrate at large scaled times. These termination types can be illustrated by detailed analysis. (Closer to near impact between the particle and substrate in particular, new physics is expected to come to the fore through the presence of significant viscous effects or through other previously negligible effects such as flow dissipation.) Most termination types are seen to be flow-dominated terminal forms, the exception being the mid-particle impact where the phase-change dynamics largely determines the physical shape involved in the impacts. In all cases, however, the complete evolution prior to the

https://doi.org/10.1017/jfm.2026.11650 Published online by Cambridge University Press

terminal forms is a full interplay involving the properties of liquid flow, phase change and particle movement.

Interestingly, the interactive system described above is found to model a different scenario, namely the case of an in-flow melting or solidifying particle close to a relatively hot or cold fixed substrate, with few modifications (as discussed in Appendix A). Each of the two scenarios, however, the rigid particle and the phase-changing one, are governed by essentially the same physical processes which bring in the three-way coupling between the flow of liquid, the phase change of the same material abutting in solid form and the free movement of the particle.

The prime application of this work is to the flow of liquid metals containing particles or impurities. The present findings may also provide a degree of insight into aerodynamic icing applications involving particles and phase change. The present model which makes use of properties at small Prandtl number seems unlikely to apply directly, however, to water flow containing ice particles, since the Prandtl number in water/ice interactions is typically on the order of ten. The icing application thus remains to be modelled.

The interaction between a phase-changing substrate and fixed particle involves many parameters. We have kept the initial conditions of the fluid flow and the particle motion fixed throughout and also concentrated on substrates which are either of the same length as the particle or shorter. If the substrate patch extends beyond the rigid-particle leading-edge and/or the trailing-edge location then the flow and thermal properties of the fluid upstream of the leading edge or downstream of the trailing edge need modification, as addressed in Liu *et al.* (2023). In contrast, for a melting or solidifying particle, allowance for variation of the leading- and trailing-edge positions with time would seem to be required when the substrate patch is sufficiently long, so as to account for melting or solidification at each particle edge.

In the case of a fixed substrate and a melting particle, a quite distinct change in flow physics is also likely to occur when the substrate centre is heated significantly, yielding a particle which is then on the verge of splitting into two parts. The difference in the lower and upper pressures locally must have a significant role in the subsequent flow evolution and its interaction with phase change and two-particle motion. For the rigid-particle case, another situation of interest is where the particle travels longitudinally relative to the wall on which substrate growth or erosion occurs, which must surely leave a residue of material in the wake of the particle's traverse. Finally here, the extremes of a small or large ratio between the fluid flow and phase-change time scales would appear well worth investigating.

The present analysis was initially conceived for ice and water flow. With the assumption of a small Prandtl number, as stated earlier in this section, the work may still indeed capture certain interactive features of melting or solidification in such systems, although its applicability is expected to be greater for materials such as solid metal particles immersed in liquid-metal flows.

Acknowledgements. The authors gratefully acknowledge the perceptive and helpful comments from the referees.

Funding. This work was supported by the Leverhulme Trust through Research Project Grant RPG-2023-233 supporting J.J.

Declaration of interests. The authors report no conflict of interest.

https://doi.org/10.1017/jfm.2026.11650 Published online by Cambridge University Press

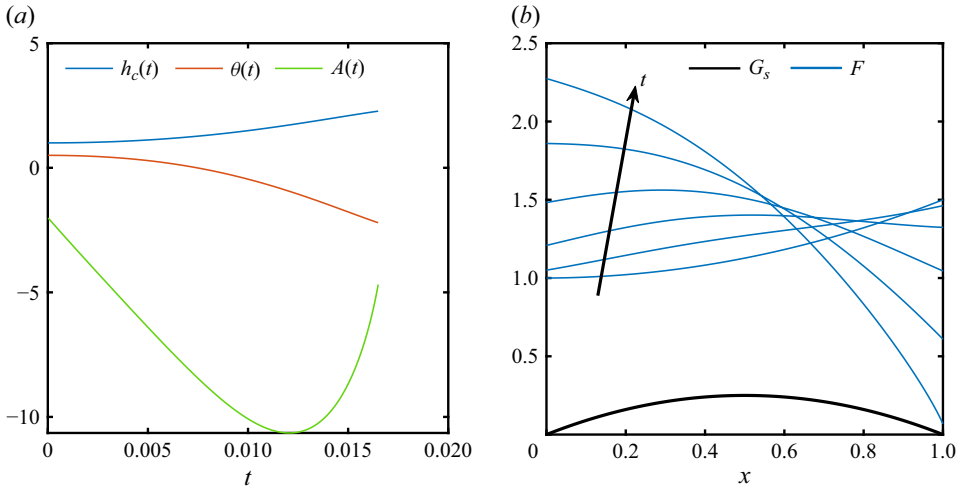


Figure 7. Numerical results of the interactive system for a phase-changing particle and fixed substrate from (3.2), but with (A1)–(A3) replacing their counterparts. Panel (*a*) shows the total lateral and rotational position, $h_c(t)$ and $\theta(t)$, and the mass flux $A(t)$. Panel (*b*) shows the substrate boundary and evolving particle underbody for six uniformly distributed times over $t = [0,\ 0.017]$. The substrate position and temperature are $G_s = x(1-x)$ and $T_s = 2x(1-x)$. The initial particle shape is $F_p(x,\ 0) = -1/2x(1-x)$, with $(h_c,\ \theta,\ v,\ \omega,\ A) = (1,\ 1/2,\ 0,\ 0,\ -2)$ and $b = 80$.

Appendix A. Application to a melting or solidifying particle

Nearly the same system as presented in § 2 is found to hold for the related interaction between a melting or solidifying particle and a rigid hot or cold substrate. The corresponding formulation has the same flow balance from (2.1) and (2.2), and pressure conditions from (2.4). In contrast, the particle underbody position $y = F$ is now

$$F = F_p(x,\ t) + h_c(t) + x\theta(t), \tag{A1}$$

where $y = F_p$ describes the particle shape, which can now vary in t due to melting or solidification. The position of the fixed, known substrate boundary is given by $y = G_s(x)$ so that the gap width satisfies $H = F - G_s$. By taking the known temperature of the fixed substrate as $\theta = T_s(x,\ t)$ and $\theta = 0$ at $y = F$, the thermal equation from (2.5) provides

$$\theta = -\frac{T_s}{H}(Y - F), \tag{A2}$$

for sufficiently small σ. The evolution of $F_p(x,\ t)$ is now given by (2.9) with F_p replacing G_s throughout, so that

$$\frac{\partial F_p}{\partial t} = b\frac{T_s}{H}. \tag{A3}$$

For a sufficiently long substrate, the presence of melting would suggest that the leading-edge and trailing-edge positions of the particle would vary, making the particle length shrink and the centre of mass move. For our specific interest, however, the heating or cooling is negligible at the leading and trailing substrate edges and hence the corresponding particle positions remain fixed at $x = 0$ or $x = 1$.

Figure 7 shows numerical simulations for a melting particle and a fixed substrate, as discussed above. We take the substrate position and temperature as $G_s = x(1-x)$ and $T_s = 2x(1-x)$, the initial particle shape as $F_p(x,\ 0) = -1/2x(1-x)$, and

https://doi.org/10.1017/jfm.2026.11650 Published online by Cambridge University Press

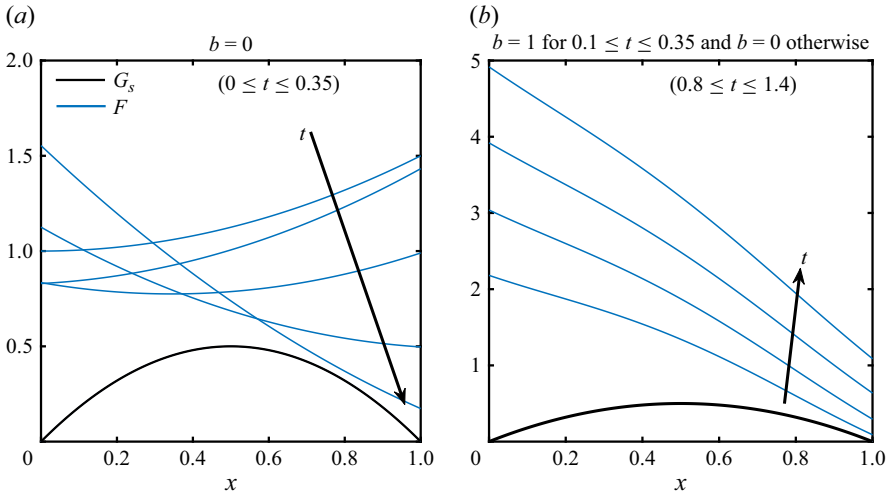


Figure 8. Numerical results of the interactive system for a phase-changing particle and fixed substrate from (3.2), but with (A1)–(A3) replacing their counterparts. The panels show the evolution of the particle underbody (and fixed substrate boundary) for $b = 0$ (a) and then $b = 1$ for $t \in [0.1,\ 0.35]$ and $b = 0$ otherwise (b). Panels (a) and (b) show F at uniformly distributed fixed times across $t = [0,\ 0.35]$ and $t = [0.8,\ 1.4]$, respectively. The substrate position and temperature are $G_s = 2x(1-x)$ and $T_s = 2$, with the latter being relevant only when $b = 1$. The initial particle shape is $F_p(x,\ 0) = -1/2x(1-x)$, and $(h_c,\ \theta,\ v,\ \omega,\ A) = (1,\ 1/2,\ 0,\ 0,\ -2)$.

$(h_c,\ \theta,\ v,\ \omega,\ A) = (1,\ 1/2,\ 0,\ 0,\ -2)$ with $b = 80$. Here, the fixed substrate is relatively hot and in consequence the particle underbody melts, creating an increasingly downwards-concave shape for increasing t. The gap width H also increases with t over the front half of the particle, but decreases substantially over much of the rear half. The evolution generates a gap closure (strictly near closure) within a finite time at the trailing-edge location, due to the absence of substrate heating there. The description of the local solution behaviour there is as given in § 4.

We now turn our attention to the scenario where particle–substrate impact can be prevented by heating the substrate on a short time interval. Substrate heating can be active or inactive by choosing $b = 1$ or $b = 0$, respectively. We take the substrate boundary as $G_s = 2x(1-x)$ and examine the isothermal case with $T_s = 2$ (the latter being relevant only when $b = 1$). The initial conditions are the same as the above example. For comparison, the particle underbody evolution is shown for the case with no substrate heating ($b = 0$) in figure 8(a), with an eventual mid-body collision occurring at $t \approx 0.38$. In figure 8(b), solutions are shown for $0.8 \leq t \leq 0.14$ with active substrate heating ($b = 1$) over the time interval $0.1 \leq t \leq 0.35$ and no heating ($b = 0$) otherwise. As seen, the short time interval over which heating is active prevents mid-body collision, with an eventual particle fly-away event occurring.

References

Batley, R.T. & Smith, F.T. 2025 Channel flow with an ice constriction: direct simulation and reduced-system analysis. *Theor. Comp. Fluid Dyn.* **39**, 34.

Bian, X. & Rangel, R.H. 1996 The viscous stagnation-flow solidification problem. *Intl J. Heat Mass Transfer* **39**, 3581–3594.

Carpenter, R. & Steen, P.H. 1997 Heat transfer and solidification in planar-flow melt-spinning: high wheelspeeds. *Intl J. Heat Mass Transfer* **40** (9), 1993–2007.

Coulson & Richardson 2019 *Chemical Engineering*, Particulate Systems and Particle Technology, 6th edn, vol. 2A. Elsevier.

https://doi.org/10.1017/jfm.2026.11650 Published online by Cambridge University Press

DINSDALE, A.T. & QUESTED, P.N. 2004 The viscosity of aluminium and its alloys – a review of data and models. *J. Mater. Sci.* **39**, 7221–7228.
DOTTO, D., SOLDATE, A. & MARCHIOLI, C. 2019 Deformation of flexible fibres in turbulent channel flow. *Meccanica* **55**, 343–356. Recent advances in modelling and simulations of multiphase flows.
FOUCAUT, J.M. & STANISLAS, M. 1997 Experimental study of saltating particle trajectories. *Exp. Fluids* **22** (4), 321–326.
GENT, R.W., DART, N.P. & CANSDALE, J.T. 2000 Aircraft icing. *Phil. Trans. R. Soc. A* **358**, 2873–2911.
GODONE, D. & STANCHI, S. 2011 *Soil Erosion Studies*. InTech.
JEPSON, J., BATLEY, R. & SMITH, F.T. 2025 Channel constriction due to wall-mounted ice growth in large Reynolds number flow. *J. Fluid Mech.* **1024**, A3.
JOLLEY, E.M. & SMITH, F.T. 2024 Free movement of a near-wall particle in fluid of comparable density. *Phys. Fluids* **36**, 107–139.
KALANTAR-ZADEH, K., RAHIM, M.A. & TANG, J. 2021 Low melting temperature liquid metals and their impacts on physical chemistry. *Accounts Mater. Res.* **2** (8), 577–580.
KATGERMAN, L. 1988 Modelling of liquid–liquid metal mixing. *Math. Comput. Model.* **10** (10), 797.
KIM, N., SCHINDLER, F., VOGT, T. & ECKERT, S. 2024 Thermal boundary layer dynamics in low-Prandtl-number Rayleigh–Bénard convection. *J. Fluid Mech.* **994**, A4.
KRISHNAMURTHI, V., *et al.* 2024 Structural evolution of liquid metals and alloys. *Adv. Mater.* **36** (30), 2403885.
KURZ, W. & FISHER, D.J. 1992 *Fundamentals of Solidification*, 4th edn. Trans Tech Publications.
LIU, Q., YAZAR, S. & SMITH, F.T. 2023 On interaction between freely moving bodies and fluid in a channel flow. *Theor. Appl. Mech. Lett.* **13**, 100413.
LOFGREN, H.B. 2001 Ideal solidi cation of a liquid-metal boundary layer flow over a conveying substrate. *J. Fluid Mech.* **446**, 121–131.
LÖFGREN, H.B. & ÅKERSTEDT, H.O. 1998 Electromagnetic braking of the flow of a liquid metal with a free surface. *Fluid Dyn. Res.* **23**, 1–25.
MOORE, M.R., MUGHAL, M.S. & PAPAGEORGIOU, D.T. 2017 Ice formation within a thin film flowing over a flat plate. *J. Fluid Mech.* **817**, 455–489.
NORDE, E. 2017 Eulerian method for ice crystal icing in turbofan engines. PhD thesis, University of Twente.
NYSTRÖM, R., REICHELT, W. & DUBKE, M. 2003 Strip casting experiences at mefos. *Scand. J. Metall.* **29**, 93–100.
OWEN, P.R. 1964 Saltation of uniform grains in air. *J. Fluid Mech.* **20** (2), 225–242.
PALMER, R.A. & SMITH, F.T. 2020 A body in nonlinear near-wall shear flow: impacts, analysis and comparisons. *J. Fluid Mech.* **904**, A32.
PEI, Z., ZHANG, Y. & ZHOU, J. 2018 A model for the particle-level simulation of multiple flexible fibres moving in a wall-bounded fluid flow. *J. Fluids Struct.* **80**, 37–58.
PURVIS, R. & SMITH, F.T. 2016 Improving aircraft safety in icing conditions. In *UK Success Stories in Industrial Mathematics* (ed. P.A. Aston, A.J. Mulholland & K.M.M. Tate), pp. 145–154. Springer.
SHAO, Y., RAUPACH, M.R. & FINDLATER, P.A. 1993 Effect of saltation bombardment on the entrainment of dust by wind. *J. Geophys. Res.: Atmos.* **98** (D7), 12719–12726.
SMITH, F.T. 2017 Free motion of a body in a boundary layer or channel flow. *J. Fluid Mech.* **813**, 279–300.
SMITH, F.T. & ELLIS, A.S. 2010 On interaction between falling bodies and the surrounding fluid. *Mathematika* **56**, 140–168.
STANKUS, S.V., SAVCHENKO, I.V. & AGAZHANOV, A.S. 2012 Thermal conductivity and thermal diffusivity of liquid indium–tin alloys. *J. Mater. Sci.* **33** (5), 774–782.
STEEN, P.H. & KARCHER, C. 1997 Fluid mechanics of spin casting of metals. *Ann. Rev. Fluid. Mech* **29**, 373–397.
VIRMAVIRTA, M., KIVEKAS, J. & KOMI, P.V. 2001 Take-off aerodynamics in ski jumping. *J. Biomech.* **34** (4), 465–470.
WILL, J.B., MATHAI, V., HUISMAN, S.G., LOHSE, D., SUN, C. & KRUG, D. 2021 Kinematics and dynamics of freely rising spheroids at high Reynolds numbers. *J. Fluid Mech.* **912**, A16.
WILSON, P.L. & SMITH, F.T. 2011 Fluid-body interactions: clashing, skimming, bouncing. *Phil. Trans. R. Soc. A* **369**, 3007–3024.
ZHANG, T., YANG, J. & JIANG, P. 2019 Measurement of molten steel velocity near the surface and modeling for transient fluid flow in the continuous casting mold. *Metals-BASEL* **9** (1), 36.
ZWIRNER, L. & SHISHKINA, O. 2018 Confined inclined thermal convection in low-prandtl-number fluids. *J. Fluid Mech.* **850**, 984–1008.

https://doi.org/10.1017/jfm.2026.11650 Published online by Cambridge University Press